AAS 21-704

DESIGN OF LOW-THRUST TRANSFERS FROM AN NRHO TO LOW LUNAR ORBITS: APPLICATIONS FOR SMALL SPACECRAFT

Beom Park,[*] Kathleen C. Howell,[†] and David C. Folta[‡]

With an expanding array of activities being examined in the vicinity of near rectilinear halo orbits (NRHOs), nearby destinations for small spacecraft are an essential component. Transfer trajectories from an NRHO to a low lunar orbit (LLO) is one such example, where the significant design challenges are associated with the low level of acceleration available to the spacecraft. A low-thrust trajectory design framework within the Earth-Moon Circular Restricted Three Body Problem is explored, utilizing a targeting problem comprised of two legs departing from the NRHO and arriving at an LLO. The performance of the devised framework is analyzed with multiple LLOs.

INTRODUCTION

Small spacecraft (s/c) are playing an increasingly important role in developing the infrastructure for cislunar operations. One example of such operations, Gateway mission, proposed by the National Aeronautics and Space Administration (NASA), is expected to deliver a hub-like facility into a Near Rectilinear Halo Orbit (NRHO) in the vicinity of the Moon.[1] Multiple missions with small s/c are under development, that either leverage an NRHO for various science objectives or support the Gateway mission. Lunar IceCube (LIC), a 6U CubeSat with a low-thrust engine, is one of the public-private partnerships selected under the Next Space Technologies for Exploration Partnerships by NASA.[2] The LIC mission, planned to launch as a secondary payload on Artemis-1, offers the capability to investigate the presence and movement of water in various forms across the lunar surface, and includes an NRHO as part of its trajectory. Another example is NASA's Cislunar Autonomous Positioning System Technology Operations and Navigation Experiment (CAPSTONE) mission, where a CubeSat is launched to the current Gateway baseline NRHO to demonstrate the navigation capability of the Cislunar Autonomous Positioning System.[3] For the LIC science objective, the mission scenario includes a transfer from the 9:2 NRHO to a highly inclined elliptic low lunar orbit (LLO).[4] A systematic strategy to accomplish this objective then also serves as the basis for other transfers to support CAPSTONE as well as other proposed scenarios. The most immediate challenge in designing such transfer trajectories is associated with the complex dynamical environment. As NRHOs only exist in a multi-body model, e.g., the Earth-Moon circular restricted three-body problem (CR3BP), the trajectory design process necessitates the consideration of gravity from, at least, both the Earth and the Moon. Another challenge results from the epoch-dependent nature of the problem. As small s/c are increasingly launched as secondary payloads, the mission timeline is subject to many potential adjustments to the launch date for the primary mission. As the orbital elements for the target LLO, for example, also depend on the epoch to satisfy the science requirements, a strategy to generate transfer trajectories between the 9:2 NRHO and a wide range of lunar orbits is required. For an impulsive engine, a number of transfer trajectory design strategies are developed by different authors,[5–7] where two impulsive maneuvers are typically introduced at the departure and the arrival to link the 9:2 NRHO to multiple LLOs. However, as a small s/c only provides a low level of acceleration, the

---

[*] Ph.D. Student, School of Aeronautics and Astronautics, Purdue University, West Lafayette, IN 47907; park1103@purdue.edu

[†] Hsu Lo Distinguished Professor, School of Aeronautics and Astronautics, Purdue University, West Lafayette, IN 47907; howell@purdue.edu

[‡] NASA Goddard Space Flight Center, Greenbelt, MD 20771; david.c.folta@nasa.gov

strategies that involve impulsive burns are not directly applicable to some small s/c scenarios. While transfers that employ low-thrust engines are introduced in the previous work,[4,6,8] the type of the destination LLOs is limited; often, the LLOs are assumed to be circular to provide solely costs estimations rather than to generate end-to-end transfers, where there are no restrictions on the orbital plane, or the strategy is verified with only a few LLOs. Accordingly, a more general strategy, that enables transfers from the 9:2 NRHO to lunar orbits associated with realistic science requirements for the LIC mission and others, is introduced in the current work.

BACKGROUNDS

A low-thrust transfer trajectory design framework is devised within the context of the Earth-Moon CR3BP. As this dynamical model incorporates the gravity of both the Earth and the Moon, it serves as a suitable environment for preliminary evaluation of transfer trajectories from the NRHO to LLOs, where the natural motion of the s/c is significantly influenced by both celestial bodies. Multiple previous investigations indicate trajectories generated within the Earth-Moon CR3BP are straightforwardly transitioned to a higher-fidelity ephemeris model.[4,9] Additionally, the low-thrust (LT) force model is integrated into the ballistic CR3BP to enable analysis of s/c trajectory with a LT engine.

The Ballistic CR3BP

The CR3BP represents a model comprised of two celestial bodies, or primaries, with a third body of infinitesimal mass. For this investigation, the primaries correspond to the Earth and the Moon. They are assumed to be centrobaric and moving in circular orbits relative to their mutual barycenter. The third body is the s/c, whose mass is negligible and, thus, does not influence the motion of the primaries. The motion of the s/c is expressed in terms of a rotating coordinate frame, represented as $\hat{x}-\hat{y}-\hat{z}$ in Figure 1, where the carets denote unit vectors. It is defined such that $\hat{x}$ coincides with the direction from the Earth to the Moon, and $\hat{z}$ coincides with $\hat{Z}$ of the inertial frame. Then, the orientation of the rotating frame with respect to the inertial frame is measured by an angle, τ, as depicted in Figure 1. The nondimensional position vector of the s/c with respect to the system barycenter, marked as B in the same figure, is defined as $\bar{r} = x\hat{x} + y\hat{y} + z\hat{z}$, where the overbars indicate vector quantities. To nondimensionalize, three characteristic quantities are defined: (i) the characteristic length, $\tilde{l}_*$, defined as the distance between the primaries, where the tilde denotes a dimensional quantity, (ii) the characteristic time, $\tilde{t}_*$, defined such that the nondimensional mean motion of the primaries is equal to one, and (iii) mass ratio, $\mu = \tilde{m}_M/(\tilde{m}_E + \tilde{m}_M)$, where $\tilde{m}_E$ and $\tilde{m}_M$ correspond to the masses of the Earth and the Moon, respectively. The set of quantities, μ, $\tilde{l}_*$, and $\tilde{t}_*$ completely define a CR3BP, where the values for the characteristic quantities are provided in Table 1. The nondimensional equations of motion for each component of the s/c in the rotating frame are,

$$\ddot{x} - 2\dot{y} = \frac{\partial U^*}{\partial x}, \quad \ddot{y} + 2\dot{x} = \frac{\partial U^*}{\partial y}, \quad \ddot{z} = \frac{\partial U^*}{\partial z}. \tag{1}$$

The dots denote the derivative with respect to the nondimensional time. The right hand terms include partial derivatives of the pseudo-potential function defined as $U^* = \frac{1-\mu}{r_{13}} + \frac{\mu}{r_{23}} + \frac{(x^2+y^2)}{2}$, where the distance between the Earth and the s/c is $r_{13} = \sqrt{(x+\mu)^2 + y^2 + z^2}$, and the distance between the Moon and the s/c is evaluated as $r_{23} = \sqrt{(x-1+\mu)^2 + y^2 + z^2}$. The differential equations in the CR3BP, as derived in the rotating frame, allow one integral of motion, i.e., an energy-like constant of motion denoted the Jacobi constant, and evaluated as $JC = 2U^* - (\dot{x}^2 + \dot{y}^2 + \dot{z}^2)$. The rotating velocity vector is defined as $\bar{v} = \dot{x}\hat{x} + \dot{y}\hat{y} + \dot{z}\hat{z}$, and the Jacobi constant is also expressed as $JC = 2U^* - v^2$ for $|\bar{v}| = v$.

Table 1: Characteristic quantities corresponding to the Earth-Moon CR3BP

Characteristic quantities	μ [n.d.]	$\tilde{l}_*$ [km]	$\tilde{t}_*$ [s]
Values	$1.2150584269940 \times 10^{-2}$	$3.847479920112920 \times 10^{5}$	$3.756998590849907 \times 10^{5}$

Five equilibrium solutions exist in the CR3BP, also termed the Lagrangian points. The location of these points are denoted L_1-L_5. Various periodic solutions of the ballistic CR3BP are known to exist in the vicinity of each Lagrangian point, where the specific family relevant to the current investigation corresponds to the halo orbit family associated with L_2. The southern members of the family are depicted in Figure 2. The 9:2 NRHO, the departure orbit for this investigation, is one member of the southern L_2 halo family of periodic orbits where the ratio of the number of orbital revolutions to the synodic period of the Moon equals 9:2. In reality, the synodic period of the Moon is not a constant value as observed from the actual ephemerides of the celestial bodies. The synodic period of the Moon is assumed to be constant in the CR3BP and for the current investigation, the value equals 29.39 days. The corresponding initial state, period, and the Jacobi constant value for the NRHO orbit of interest are listed in Table 2. This definition of the 9:2 NRHO in the CR3BP is consistent with a previous investigation by Zimovan-Spreen,[10] resulting in the same Jacobi constant value, $JC_{NRHO} \approx 3.04719$.

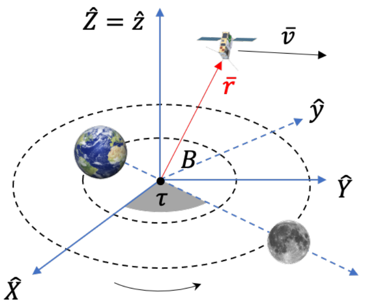

Figure 1: CR3BP (image credit: NASA)

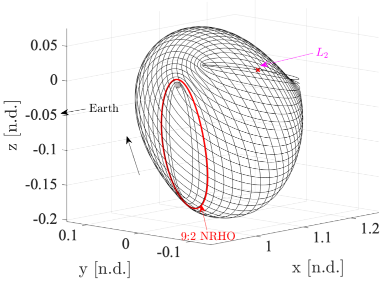

Figure 2: L_2 Southern halo orbit family

Table 2: 9:2 NRHO data

	x_0 [n.d.]	y_0 [n.d.]	z_0 [n.d.]	$\dot{x}_0$ [n.d.]	$\dot{y}_0$ [n.d.]	$\dot{z}_0$ [n.d.]	P [n.d.]	P [days]	JC [n.d.]
Values	1.021335	0	-0.181619	0	-0.101756	0	1.502061	6.53	3.047188

Low-Thrust Force Model and CR3BP-LT

The motion of a s/c with a LT engine is governed by (i) the engine parameters, including the maximum level of thrust ($\tilde{T}_{max}$) and the specific impulse ($\tilde{I}_{sp}$), and (ii) the spacecraft parameters involving the available power and the mass of the s/c ($\tilde{m}$). In general, engine parameters are functions of the available power. However, they are assumed to be constant in the current investigation; as the available power depends on the distance of the s/c from the Sun, it is reasonable to approximate the distance as a constant value in cislunar space. To incorporate the acceleration that the engine imparts on the s/c into the ballistic CR3BP, the thrust, specific impulse and s/c mass are nondimensionalized utilizing $\tilde{l}_*$, $\tilde{t}_*$, and $\tilde{m}_0$, where $\tilde{m}_0$ denotes the initial dimensional mass of the s/c. Then, the LT acceleration term is computed as, $\bar{T}/m$, where $\bar{T}$ and m are the nondimensional LT force vector and mass of the s/c, respectively. Since m also changes as the s/c consumes propellant, the Eq. (1) is updated as follows,

$$\ddot{x} - 2\dot{y} = \frac{\partial U^*}{\partial x} + \frac{T_x}{m}, \quad \ddot{y} + 2\dot{x} = \frac{\partial U^*}{\partial y} + \frac{T_y}{m}, \quad \ddot{z} = \frac{\partial U^*}{\partial z} + \frac{T_z}{m}, \quad \dot{m} = -\frac{T}{g_0 I_{sp}} \tag{2}$$

where T_x, T_y, T_z denote the LT force components in the directions of $\hat{x}, \hat{y}, \hat{z}$, respectively. The magnitude of the nondimensional thrust vector, $|\bar{T}| = T = \sqrt{T_x^2 + T_y^2 + T_z^2}$, is between 0 and T_{max}, the nondimensional maximum level of thrust. The mass flow rate is computed with the nondimensional specific impulse, I_{sp}, and g_0, the nondimensional value for the standard gravity acceleration $\tilde{g}_0 = 9.80665 m/s^2$. The LT parameter values in the current investigation are listed in Table 3 in the dimensional units. This set of values are consistent with the Lunar IceCube s/c.

Table 3: Low-thrust related parameter values

Low-thrust parameters	$\tilde{m}_0$ [kg]	$\tilde{I}_{sp}$ [s]	$\tilde{T}_{max}$ [mN]
Values	13.6	2156	1.1

Control Laws

Describing the motion of s/c within the CR3BP-LT model is challenging as it incorporates a control problem; the history of the s/c states is coupled with the history of the control variable, i.e., the thrust magnitude and direction at each moment along the trajectory. One approach is a set of control laws that mathematically govern the thrust magnitude and direction. For example, Cox et al.[11] utilize a control law that assumes a constant thrusting direction in the rotating frame, with the maximum thrust level, to compute additional dynamical structures that exist within the CR3BP-LT model. In the current investigation, two different control laws, based on the Jacobi constant, are employed. The anti-velocity law (Figure 3(a)) assumes that the thrusting direction is opposite to the rotating velocity vector of the s/c, $\bar{v}$, and the pro-velocity law (Figure 3(b)) is based on a thrusting direction that is aligned with the rotating velocity vector. Although different levels of thrust are evaluated in each case, when $T = T_{max}$, these laws represent time-optimal control laws that most efficiently adjust the Jacobi constant value within the CR3BP; for a desired increase in the Jacobi constant, the anti-velocity law delivers it with the minimum duration, and vice versa for the pro-velocity law. It is noted that these control laws are defined with the velocity components in the rotating frame as the energy within the CR3BP is characterized by the Jacobi constant that is computed with the rotating velocity components. Accordingly, control laws that optimally change the Jacobi constant are suitable when a considerable variation in the energy level along a trajectory is expected.[12]

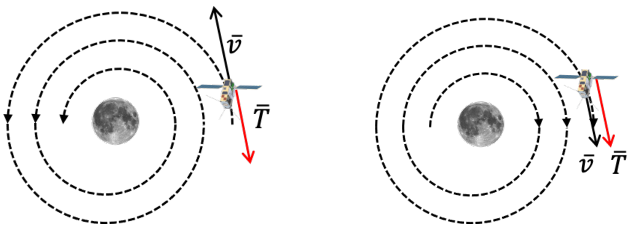

(a) Anti-velocity law (b) Pro-velocity law

Figure 3: Control laws utilized in the current investigation - $\bar{v}$ represents the rotating velocity vector

State Transformation

While the departure NRHO is periodic when it is viewed from the rotating frame, the arrival LLOs of interest exist at low altitudes above the Moon and are best illustrated within a Moon-centered inertial frame. Rather than the Cartesian state components, the orbital elements are often utilized to approximate the six dimensional state that fully characterizes the arrival LLO.[4,9] In the current investigation, states are expressed in terms of the rotating frame as $\bar{r}$ and $\bar{v}$, while osculating Keplerain elements with respect to the Moon, œ, are utilized as a complementary representation. The six components of œ correspond to the semi-major axis (a), eccentricity (e), inclination (i), right ascension of the ascending node (RAAN, Ω), argument of periapsis (AOP, ω), and true anomaly (TA, ν). Note, however, that each component of œ does not stay constant within the CR3BP as it only corresponds to a hypothetical conic computed with a state vector within the CR3BP associated with a certain epoch. Still, two states within the CR3BP may be compared with their corresponding œ, especially when the s/c is under a great influence of the Moon's gravity; the osculating elements serve as preliminary approximations that help define the distance between two states, which is a necessary component in generating a suitable initial guess for gradient-based methods.

To facilitate analysis, a standard transformation between states in the rotating frame, $\bar{r}$ and $\bar{v}$, and in Keplerian elements, œ is evaluated. The transformation from $\bar{r}, \bar{v}$ to œ involves an intermediate frame rotation between the rotating and the Moon-centered inertial frames. Figure 4 illustrates the transformation process, where C denotes the transformation function with superscripts indicating the state in the rotating frame (R), state in the inertial frame (I), and state in terms of osculating Keplerian elements (œ). Note that the transformation between the rotating and the inertial frame, ${}^{R}C^{I}$ or ${}^{I}C^{R}$, requires the information about the instantaneous angle, τ, defining the orientation of the rotating frame with respect to the inertial frame that takes any value between $0°$ and $360°$. This angle is also termed the "epoch" as it denotes the CR3BP orientation of the Earth and the Moon relative to a reference inertial frame. Although the second transformation between the inertial frame and Keplerian elements, ${}^{I}C^{\text{œ}}$ or ${}^{\text{œ}}C^{I}$, does not require the epoch information, the transformation indirectly depends on the epoch, τ. More specifically, all of the elements are independent of the epoch but the RAAN angle, Ω. Consider two sets of orbital elements, œ_1 and œ_2, that coincide except for the RAAN angles that satisfy $\Omega_1 = \Omega_2 + \Delta\Omega$. Denoting the states in the rotating frame after the transformation as $(\bar{r}_1, \bar{v}_1)$ and $(\bar{r}_2, \bar{v}_2)$, two sets of rotating states coincide if and only if the epochs associated with the transformation, i.e., τ_1 and τ_2, satisfy $\tau_1 = \tau_2 + \Delta\Omega$. Or, the following relationship,

$$\Omega_1 - \tau_1 = \Omega_2 - \tau_2, \tag{3}$$

must be satisfied to result in the same rotating state after the transformation, and vice versa.

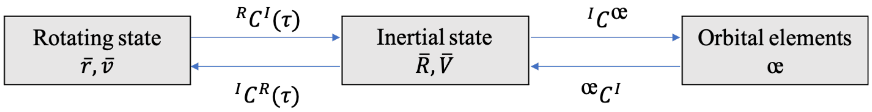

Figure 4: State transformation between the rotating frame and Keplerian elements

FRAMEWORK

A trajectory design framework that is capable of producing LT transfer trajectories from the NRHO to different arrival LLOs is introduced. A targeting problem is formulated, where gradient-based methods are utilized to solve for fully continuous, feasible solutions and to eventually produce optimal trajectories. The success of any gradient-based methods depends heavily on the quality of the initial guess; it is required to be sufficiently close enough to a local basin of solutions to gradually locate a solution. Accordingly, initial guess strategies suitable for the proposed targeting problem are introduced.

Problem Formulation

In a LT problem, the trajectory design typically leverages the evolution of the energy level associated with the s/c state along a transfer arc. Recall that the energy of the s/c state in the ballistic CR3BP is characterized by the Jacobi constant value, JC. The 9:2 NRHO is associated with a value $JC_{NRHO} \approx 3.05$, whereas a typical LLO corresponds to a much higher Jacobi constant, $JC_{NRHO} >\approx 4$. As the capability of a LT engine provides a continuous change of the JC, any value of the JC between JC_{NRHO} and JC_{LLO} is passed at some point along the transfer path. An intermediate value of $JC = 3.3$ is selected to decompose the transfer trajectory design problem into two distinct phases, as reflected in Figure 5. Two legs before and after the interface are denoted the "NRHO leg" and the "LLO leg" and are plotted as orange and brown arrows in Figure 5, respectively. Then, explicit propagations of Eq. (2) in forward time from the NRHO and backwards in time from the LLO are blended to construct two continuous legs that departs from the NRHO and arrives at the LLO, respectively. The directions of the integration are illustrated as red arrows in Figure 5. Note that this formulation ensures that the initial guess is fully continuous along the whole transfer arc except for the interface location; a gap in the seven dimensional s/c state including the position, velocity, and mass, exists. Then, a key to generating a viable initial guess is equivalent to selecting a pair of legs with a minimal gap at the interface, one that is small enough to be bridged by a gradient-based method. In subsequent sections, the control laws for each leg are detailed.

It is noted that different formulations for the problem are also suitable for constructing transfer arcs. Backwards propagation from an LLO is introduced, however, to overcome the challenge associated with such a low-level of thrust that only supplies limited control authority to deliver the s/c trajectory. Solely relying on forward propagation requires a strategy specifically designed for a many-revolutions trajectory. Such strategies are often formulated upon an implicit assumption that the “perturbing" forces beyond the gravitational force from the central body are negligible compared to the LT engine force. When this assumption no longer holds, the convergence behavior for such strategies is not guaranteed. For example, the Q-law guidance scheme[13] produces the “optimal" thrusting direction to drive a candidate Lyapunov cost function to zero, then reaching the target LLO. When the thrust level is only marginally greater than any perturbing forces, however, convergence to the target orbit may not, in fact, be achieved. Of course, the Q-law strategy can be very effective as accomplished in previous investigations to generate Mars-centered spiral-down arcs for exploration of the Martian moons[14] and also selenocentric arcs for cislunar applications.[15] However, the same strategy is less efficient in the current investigation due to the lower level of acceleration available from the engine, $8 \times 10^{-5}\mathrm{m}/s^2$, as compared to $3 \times 10^{-4}\mathrm{m}/s^2$ found in the literature.[15]

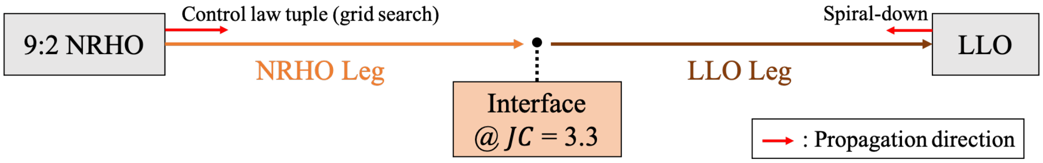

Figure 5: Schematic for the targeting problem

NRHO Leg

Suitable strategies are required to construct the NRHO leg that departs from the NRHO but also maintains a captured motion near the Moon with the potential to connect to the LLO leg. Generating transfer trajectories from the NRHO to different potential destinations is an ongoing area of research, both using impulsive maneuver and LT forces; various authors propose different strategies to depart the periodic orbit. For one such example, the dynamical structures that exist in the ballistic Earth-Moon CR3BP are leveraged. Zimovan[10] utilizes the unstable manifolds from the NRHO to construct transfer trajectories to nearby periodic orbits. Pritchett[9] as well as Prado Pino et al.[4] suggest that a chain of periodic orbits near the NRHO are useful for producing LT trajectories departing from the NRHO as energy levels evolve. Other examples include the introduction of impulsive burns in various directions to depart the NRHO. Based on these impulsive departure burns, Davis et al.[16] analyze the resulting destination for different trajectories that depart from the NRHO. Similarly, Lu et al.[7] investigate direct transfer options between the NRHO and LLOs with two impulsive burns. Muralidharan[17] suggests similar transfer options but leverages the information concerning the most-stretching direction in the local flow.

Transfer trajectories in this regime that involve impulsive burns are not easily transitioned to LT trajectories, particularly for very low thrust levels. The impulsive magnitude is too large to be produced by the LT engine, and already requires multiple revolutions around the Moon to meet the required change in energy via the change in speed. For example, a small impulsive burn with magnitude of 10m/s requires approximately 1.5 days of continuous thrusting with the current LT parameters in Table 3. Thus, the analysis of the impulsive burn trajectories offers limited insight for the current purposes. Moreover, the LT transfer trajectory problem also requires an initial guess for the control history, that consists of the magnitude of the thrust as well as the direction. While previous investigations[4,9] succeed in generating LT trajectories originating from the NRHO, the initial guess for the control is limited. Such approaches typically rely on the gradient-based methods to generate the control history, and the result often exhibits a complex and random behavior that is difficult to systematically understand and exploit. This deficiency hinders the goal of the current investigation to develop a general framework.

To overcome some of the challenges associated with the departure from the NRHO, a set of control laws are employed that are based on the heuristics regarding the energy level of the s/c state. Recall that within the CR3BP, increase in the Jacobi constant level corresponds to decrease in the energy, and vice versa. For simplicity, it is assumed that only three kinds of behavior are available: (i) anti-velocity law to decrease the energy, (ii) pro-velocity law to increase the energy, and (iii) ballistic motion with a zero thrust level for a path at a constant energy level. While it is natural to decrease the energy of the s/c state to close the energy gap between the NRHO and an LLO, doing so without any preceding arc from the NRHO only results in a trajectory that impacts the lunar surface due to the small perilune distance that defines the NRHO. Thus, initially, the energy must be increased, followed by the anti-velocity propagation to decrease the energy.

To generate transfer options using these control laws, three variables, t_1, t_2, and t_3, are introduced. The first variable, t_1 corresponds to the departure location along the 9:2 NRHO, measured as the time passed from the apopasis.[16] Next, from departure, t_2 denotes the duration of the propagation arc with the pro-velocity law. Finally, t_3 corresponds to the ballistic propagation, i.e., coast, before the anti-velocity law is employed until the JC of the spacecraft state satisfies $JC = 3.3$. This intermediate ballistic arc expands the departure options. Under this definition of the departure arc, any NRHO leg is fully characterized by a tuple $\mathbf{S} = (t_1, t_2, t_3)$. Then, to systematically search for different departure options, a $500 \times 500 \times 500$ grid is formulated, where t_1 is equally divided between 0 and P, the period of the 9:2 NRHO, and t_2 and t_3 are decomposed into segments between 0 and 10 days.

The final s/c state at the end of the propagation arc with the anti-velocity law is recorded and classified into four categories: (i) escape from the lunar vicinity on the L_1 side, (ii) escape from the lunar vicinity on the L_2 side, (iii) impact into the lunar surface, and (iv) capture. The tuples that result in capture are recorded, along with the length of the anti-velocity propagation arc in time until the interface, denoted $t_{D,N}$, as well as the s/c state at the interface that includes the osculating elements (œ$_N$) and mass (m_N). The subscript N denotes the variables that correspond to the NRHO leg. For the transformation of the rotating state into œ$_N$, the epoch is assumed to be $\tau = 0°$, an assumption that is later adjusted. The grid results in $125,000,000$ points to be investigated, where the numerical integration is conducted within a C++ function, mexed with a MATLAB script. The ratio of the tuples that result in capture is approximately 2.7%, providing three million candidate NRHO legs. The remaining arcs consist of 5.3%, 49.3%, and 42.7% for L_1 escape, L_2 escape, and impact, respectively. It is possible that the escape trajectories return to the vicinity of the Moon, resulting in exterior transfer trajectories. For the current investigation, however, the scope is limited to the interior transfers, where the s/c remains in the vicinity of the Moon throughout the transfer.

All the capture tuples are depicted in Figure 6(a), where x, y, and z axes correspond to t_1/P, t_2, and t_3 values. Five values for t_1/P are marked as planes with different colors in the same plot for instance. These values correspond to different departure locations along the NRHO, as indicated in Figure 6(b). Note that $t_1/P = 0$ and $t_1/P = 1$ denote the same departure location due to the periodicity of the NRHO. Contour plots in Figures 6(c)-6(f) illustrate the population of different categories for the end states resulting from $\mathbf{S}$. It is noted that the capture tuples only exist as “transient" behavior, surrounded by either escape or impact tuples. The geometry of the four trajectories corresponding to the tuples marked in Figure 6(d) is illustrated in Figure 7.

It is noted that the currently introduced set of control laws do not represent the infinitely possible departure options from the NRHO; rather, they correspond to only a subset with simple laws based on the evolution of energy as defined by the value of Jacobi constant in the CR3BP. Also, if desired, additional numbers of intermediate arcs may be introduced to expand the search space. Similarly, the data set for the NRHO legs is also extended by using longer time intervals for t_2 and t_3. For the current investigation, the data set for NRHO legs are generated such that $T = 0.9T_{max}$, or the thrust level is assumed to be only 90% of the maximum value for the control laws. This modification is integral for the subsequent gradient-based methods to converge the targeting problem; otherwise, the methods often fail to produce feasible solutions as the thrust level is saturated to the maximum possible level. Different levels of thrust may be implemented to construct various data set.

LLO Leg

The anti-velocity law is assumed for the control history to construct the LLO leg. Although this simple control law cannot target a specific LLO by propagating in forward time from the interface, it is coupled with

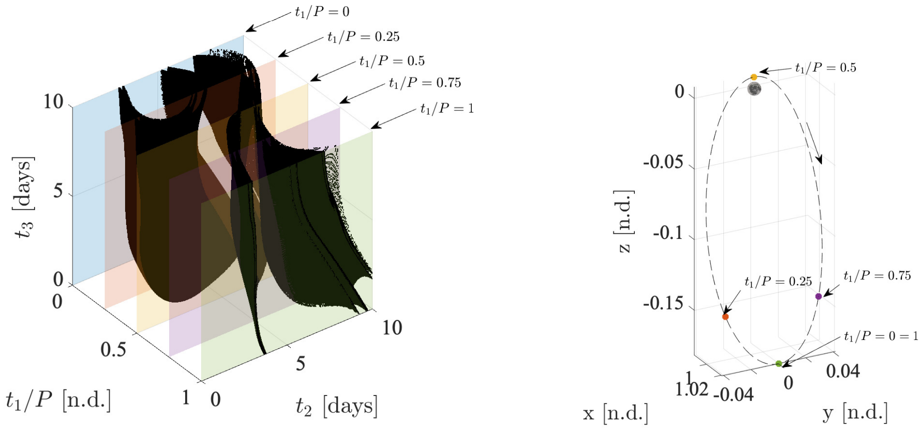

(a) Capture tuples (b) Illustrative departure locations

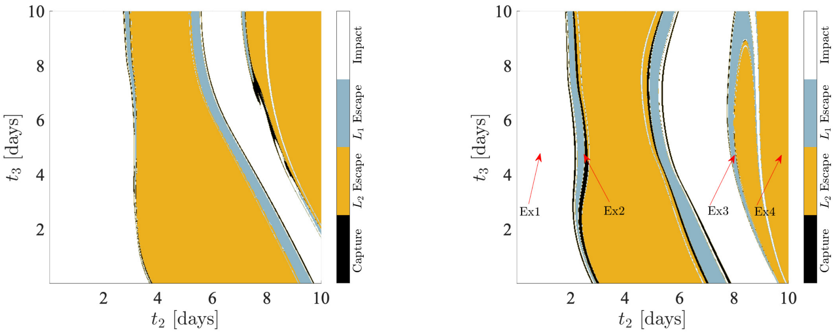

(c) Contour plot for $t_1/P = 0 = 1$ (d) Contour plot for $t_1/P = 0.25$

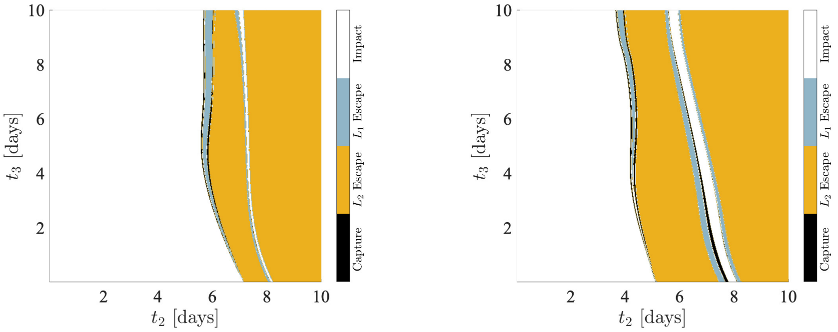

(e) Contour plot for $t_1/P = 0.5$ (f) Contour plot for $t_1/P = 0.75$

Figure 6: End state categories from **S** to properly depart the NRHO

the backwards propagation from the LLO to ensure the desired arrival at the LLO. The thrust magnitude is maintained at the maximum possible value along the spiral-down trajectory. For simplicity, it is assumed that an LLO is fully characterized by six variables that include the epoch upon the arrival, τ_F, and all components of $œ_F$ except for the TA angle, ν_F; within the CR3BP, these variables only approximate an LLO at a certain instant, as the osculating values depend on the epoch as well as the TA angle. Given these 6 variables of an LLO, the LLO leg generated with the backwards propagation is fully characterized by three additional parameters: (i) the mass upon the arrival, m_F, (ii) the arrival location at the LLO, ν_F, and (iii) the length of the propagation with the anti-velocity law, $t_{D,L}$.

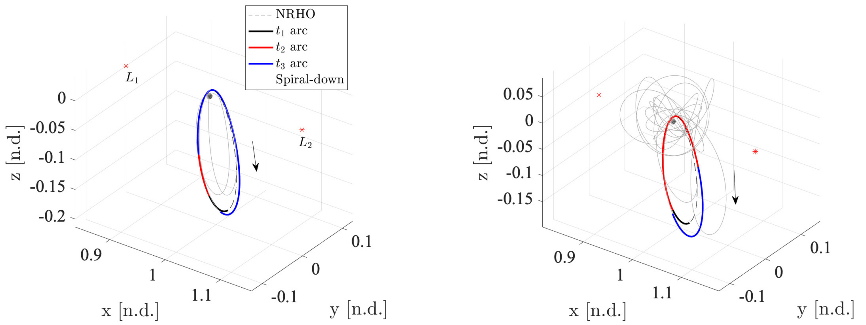

(a) Impact trajectory example (Ex1 from Figure 6(d)) (b) Capture trajectory example (Ex2 from Figure 6(d))

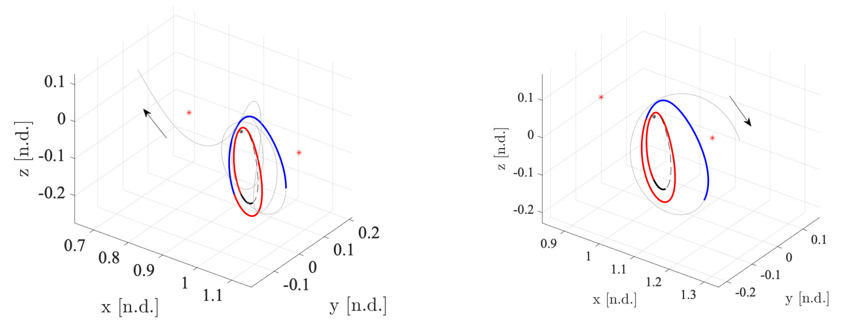

(c) L_1 escape trajectory example (Ex3 from Figure 6(d)) (d) L_2 escape trajectory example (Ex4 from Figure 6(d))

Figure 7: Geometry of the trajectories corresponding to different categories

Steps

The steps illustrated by the schematic in Figure 8 are executed to merge two legs into a continuous transfer trajectory within the CR3BP. Boxes on the left column denote the steps, where different colors indicate different phases in the algorithm. From the user inputs (red), the initial guess is generated (blue), followed by solving for a feasible trajectory (green) as well as an optimal trajectory (brown).

Inputs [A1] The fixed inputs consist of (i) the data set for the NRHO departure generated with tuple $\mathbf{S}$, (ii) τ_F, and (iii) œ_F of the target LLO except for ν_F. The inputs also include initial values for ν_F and m_F that correspond to the additional spiral-down parameters for the LLO leg. These variables are initialized to be $\nu_F = 0°$ and $m_F = 0.95$n.d., without losing any generality, but are subject to change within the subsequent steps.

Initial Guess Generation [B1-B6] It is integral for the algorithm to generate an initial guess that results in minimal infeasibility, including discontinuities in the state history, and violation of the terminal constraints as well as the control bounds. From the problem formulation introduced in Figure 5, the initial guess that combines the NRHO and LLO legs are already feasible except at the interface; a discontinuity between two legs exists, comprised of three position components, three velocity components, and the mass. Thus, the steps within the initial guess generation phase are employed to minimize the discontinuity that exists for each of the components in a seven dimensional state vector. At the interface, the position and velocity state components, $\bar{r}$ and $\bar{v}$, from both legs are represented with corresponding osculating orbital elements, œ. The epoch at the interface is computed as $\tau_I = \tau_F - t_{D,L}$ and utilized for the state transformation. Then, eliminating the discontinuity that exists for the rotating state components is identical to removing the difference of the osculating orbital elements at the interface. While the osculating elements never stay constant within the ballistic CR3BP, they are able to partially characterize the s/c state at this particular energy level, $JC = 3.3$,

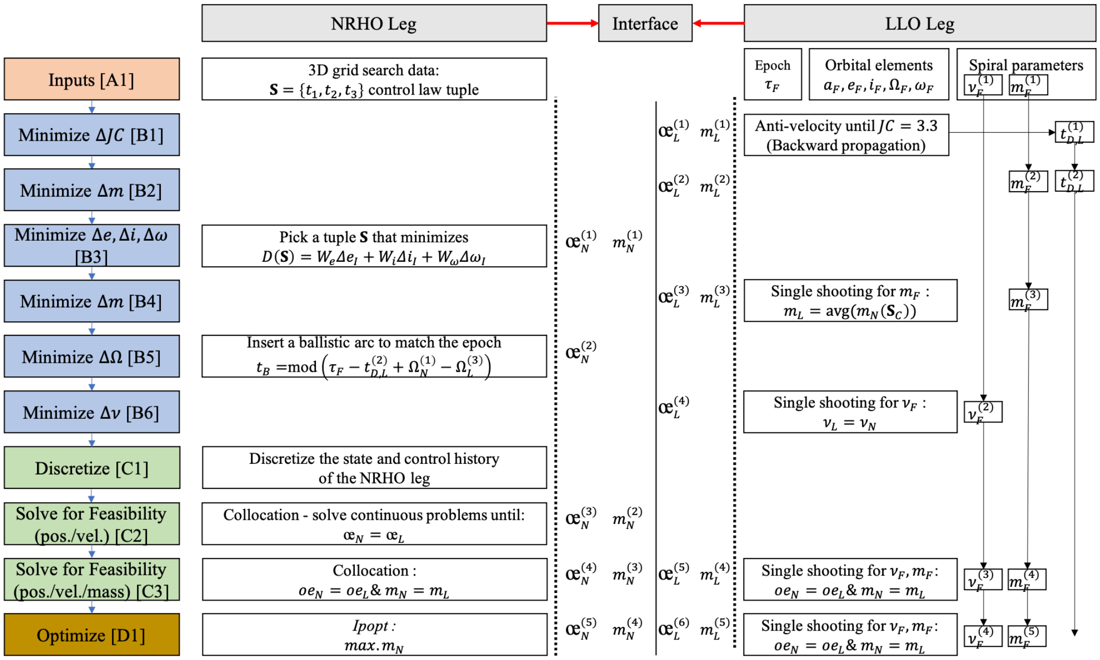

Figure 8: A schematic of the steps within the framework

where the s/c displays a captured motion in the vicinity of the Moon to some amount. This complementary representation enables a series of steps, where parts of discontinuity in 7D state components are gradually resolved at each step, rather than simultaneously comparing all 7D components. Sequentially minimizing the errors that exist in each component of œ and m, an initial guess associated with a moderate discontinuity at the interface is located; the same strategy is not readily available with the state represented in the rotating frame as $\bar{r}$ and $\bar{v}$. Again, it is emphasized that œ is only an alternative representation of the state within the CR3BP under a certain epoch, and does not stay constant within the CR3BP. Note that using a specific order for the steps is necessary for the algorithm to achieve the desired result, as some state components are dependent on the other components. The superscripts for œ, m, ν, and $t_{D,L}$, are initialized to be "(1)", and are incremented whenever the corresponding quantities are updated. The order of the steps is as follows:

- [B1] The anti-velocity law is utilized to generate the LLO leg with backwards propagation. Note that among three parameters that characterize the leg, $\nu_F^{(1)}$ and $m_F^{(1)}$ are initialized by the user, but the length of the propagation, $t_{D,L}$, is yet unspecified. The anti-velocity propagation is continued until the Jacobi constant corresponding to the s/c state reaches the value $JC = 3.3$, where the corresponding length of the propagation is recorded as $t_{D,L}^{(1)}$. At the end of the backwards propagation, the orbital elements and mass are retrieved as $œ_L^{(1)}, m_L^{(1)}$ with the epoch of $\tau_I = \tau_F - t_{D,L}$.

- [B2] A targeting subproblem is solved to locate the arrival mass, m_F, that satisfies the following constraint at the interface,

$$m_L - \text{avg}(m_N(\mathbf{S}_C)) = 0, \tag{4}$$

  where "avg" denotes the mean function, and $\mathbf{S}_C$ represents the set of control tuples illustrated as black dots in Figure 6(a), that result in captured motion around the Moon. While different capture trajectories are associated with various interface mass values, m_N, the value for m_F is adjusted such that the mass value of the LLO leg at the interface is matched with the average value from the NRHO leg to prevent a large discontinuity in the mass values in subsequent steps. As a result of this process, the orbital elements and mass of the LLO leg at the interface are updated to $œ_L^{(2)}$ and $m_L^{(2)}$, respectively. Similarly, $t_{D,L}$ is updated to $t_{D,L}^{(2)}$ as it requires different duration of propagation to reach $JC = 3.3$ with a different value for the final mass, $m_F^{(2)}$.

- [B3] The control law tuple, $\mathbf{S}$, of the NRHO leg that minimizes the following distance function is selected from the data set,

$$D(\mathbf{S}) = W_e \Delta e + W_i \Delta i + W_\omega \Delta \omega = W_e |e_N - e_L| + W_i |i_N - i_L| + W_\omega |\omega_N - \omega_L|, \tag{5}$$

  where W denotes the weight for each component with e represented in nondimensional unit and i, ω represented in radians. Throughout the current investigation, $W_e = W_\omega = 1$, $W_i = 5$ are utilized to mirror the fact that the orbital elements corresponding to the orbital plane, i and Ω are relatively difficult to change once the s/c is captured by the lunar gravity. The selected $\mathbf{S}$ and the corresponding NRHO leg determines the error of the e, i, and ω that exists between two legs. The orbital elements and the mass at the interface for such $\mathbf{S}$ are denoted $œ_N^{(1)}$ and $m_N^{(1)}$, respectively.

- [B4] Another targeting subproblem is solved to search for the final mass that results in the mass continuity at the interface. As a result, the orbital elements are updated to be $œ_L^{(3)}$, the mass at the interface is updated to be $m_L^{(2)} = m_N^{(1)}$. Note that this step assumes the same duration of the propagation for the LLO leg.

- [B5] Up to this point, the Ω angle of the NRHO leg at the interface is computed by assuming the epoch is zero, $\tau = 0°$. Without additional adjustment, due to the discontinuity in the epoch, the NRHO leg and LLO leg are interfaced at orbital planes with different orientations. This disparity is mitigated by inserting a ballistic phasing arc, where the length of the ballistic arc is computed by,

$$t_B = \text{mod}(\tau_F - t_{D,L}^{(2)} + \Omega_N^{(1)} - \Omega_L^{(3)}, 2\pi), \tag{6}$$

  following Eq. (3). The modular operator “mod" ensures that the length of the additional ballistic arc is kept between 0 and 2π. As a result of this operation, $œ_N$ is updated to $œ_N^{(2)}$, as œ slightly change along the ballistic CR3BP arc due to the perturbing effects from the Earth. The mass of the NRHO leg at the interface stays the same after this step as the ballistic arc does not consume the propellant.

- [B6] Finally, another targeting subproblem is formulated to solve for a final true anomaly, ν_F, that ensures the continuity of ν at the interface. As a result of this operation, $œ_L$ is updated to be $œ_L^{(4)}$, where $\nu_L^{(4)} = \nu_N^{(4)}$. As the true anomaly is the “fast" variable that changes in the greatest amount for a given time, discrepancy in the true anomaly is not handled easily in the subsequent gradient-based methods. Thus, for securing an initial guess with the continuity of true anomaly, deviations in other orbital elements ($œ_L^{(3)} \rightarrow œ_L^{(4)}$) are tolerated.

The discrepancy at the interface, measured as a seven dimensional vector consisting of the osculating orbital elements as well as the mass value, is finalized after these steps. The success of the following corrections steps utilizing gradient-based methods depends on this 7D error vector. Note that the semi-major axis, a, is not considered during the initial guess generation phase as it is implicitly targeted by assuming $JC = 3.3$ at the interface. As both quantities measure the energy of the spacecraft state, a need not be explicitly targeted during this initial guess generation phase.

Feasibility Solver [C1-C3] The 7D discrepancy at the interface is removed by following steps within the feasibility solver phase.

- [C1] The NRHO leg from the initial guess consists of the forward propagation generated with the selected control law tuple $\mathbf{S}$, followed by the ballistic propagated arc with length t_B computed from Eq. (6). The history of the state and control for the NRHO leg is first discretized as required by gradient-based methods. While there exist multiple options for gradient-based methods, the fixed-time direct collocation algorithm is utilized, that is explained by Pritchett[9] and Park.[18] A collocation scheme discretizes a continuous trajectory into s segments. Within each segment, the dynamics are approximated with 7^{th} order polynomials to result in 12^{th} order integration with the Legendre-Gauss-Lobatto node placement scheme. The length of each segment is fixed within the collocation scheme. Then, a design vector is formulated that combines the discretized state as well as control. The states are represented within the Earth-Moon CR3BP rotating frame. The control is assumed to be constant in both magnitude and direction over each segment. The direction is expressed within a rotating VNC frame, where the unit vectors of the frame are computed as $\hat{v} = \bar{v}/v$, $\hat{n} = (\hat{r} \times \hat{v})/|(\hat{r} \times \hat{v})|$, and $\hat{c} = \hat{v} \times \hat{n}$. The discretized state and control histories are represented in Figure 9(a) in the rotating frame. The states are plotted as red dots, and the control vector over each segment is illustrated as red arrows. Then, a design vector that satisfies the constraints is located by a Newton-Raphson scheme,[9] one of gradient-based methods. The dynamics represented by Eq. (2) is enforced by matrix algebra within collocation, while additional terminal constraints are incorporated to ensure the continuity at the interface between both legs. Note that the LLO leg is not discretized and remains to be parametrized by three parameters, ν_F, m_F, and $t_{D,L}$, to reduce the size of the problem and also the overall computation time. Utilizing an intermediate Jacobi constant that is larger than 3.3 is associated with a longer NRHO arc and thus a larger size of the problem; the value of $JC = 3.3$ is selected to result in a moderate problem size while allowing complementary representation of s/c state with osculating elements.

- [C2] For a set of fixed values of $\nu_F = \nu_F^{(2)}$, $m_F = m_F^{(3)}$, and $t_{D,L} = t_{D,L}^{(2)}$ for the LLO leg, the gradient-based method is utilized to locate the NRHO leg that results in position and velocity continuity at the interface. As a result of this step, $\text{œ}_N = \text{œ}_L$ is satisfied. It is noted that as the collocation scheme utilizes the states represented within the rotating frame, this condition is actually reached by the corresponding rotating states, i.e., $(\bar{r}_N, \bar{v}_N) = (\bar{r}_L, \bar{v}_L)$, within the algorithm. The gap at the interface located by the initial guess is often too large for a solver to locate a feasible solution. Here, a continuations scheme is utilized to solve for intermediate œ values that gradually approach the target values of œ_L. The original error vector is computed as $\Delta\text{œ} = \text{œ}_L^{(4)} - \text{œ}_N^{(2)}$. Then, instead of abruptly enforcing $\text{œ}_L^{(4)} = \text{œ}_N^{(2)}$ as the terminal constraints, intermediate orbital elements are defined as $\text{œ}_{I,i} = \delta \cdot \Delta\text{œ} \cdot i + \text{œ}_N^{(2)}$ for $1 \leq i \leq 1/\delta$, where δ denotes the ratio of the distance progressed by each intermediate problem compared to the original error. The value of $\delta = 1/10$ is utilized, which requires solving for 10 problems to finally arrive at the desired orbital elements at the interface. If the solver fails to deliver a feasible solution within a maximum number of iterations set by the user, 30 in the current investigation, δ is halved and another attempt takes place. If this value is below a user-defined tolerance value, $\delta = 1/80$, for example, it is defined as failure. To illustrate, zoomed-in view near the interface between two legs of Figure 9(a) is provided in Figure 9(b). The end of the NRHO leg, corresponding to $\text{œ}_N^{(2)}$, is distanced from the black dot, denoting $\text{œ}_L^{(4)}$, or the beginning of the LLO leg. As this gap between two states is too large to be overcome within single problem, multiple problems are constructed that gradually move the terminal state of the NRHO leg to $\text{œ}_{I,i}$, marked as green dots in the same plot.

- [C3] The reason for separating the mass from the original corrections process is the sensitivity. As the parametrized LLO leg depend on only three parameters and involve multiple revolutions around the Moon, even a small change of the parameters result in large amount of variations at the interface. After obtaining a feasible solution that results in the continuity in position and velocity from [C2], another step is employed to target the intermediate mass continuity by adjusting the final mass value, while simulataneously satisfying all the constraints for the NRHO leg.

Optimizer [D1] Finally, the optimizer is utilized to obtain a propellant optimal solution with the same time of flight obtained from the previous steps. The optimization step is preceded by solving for the feasible solution, as existence of the latter indicates the existence of a local basin of feasible solutions. As optimization tends to require significantly more computation time compared to solving for feasible solutions, ensuring the existence of solution greatly reduces the overall computation time. In the current investigation, maximizing the mass value at the interface is defined as the optimization. The collocation scheme is paired up with an open-source optimizer, *ipopt*.[19] Similarly from the discussions above, the multiple-revolutions around the Moon for the LLO leg prohibit the optimizer to aggressively search for an optimal solution that improves the propellant consumption by a large amount compared to the feasible solution. The optimality of the

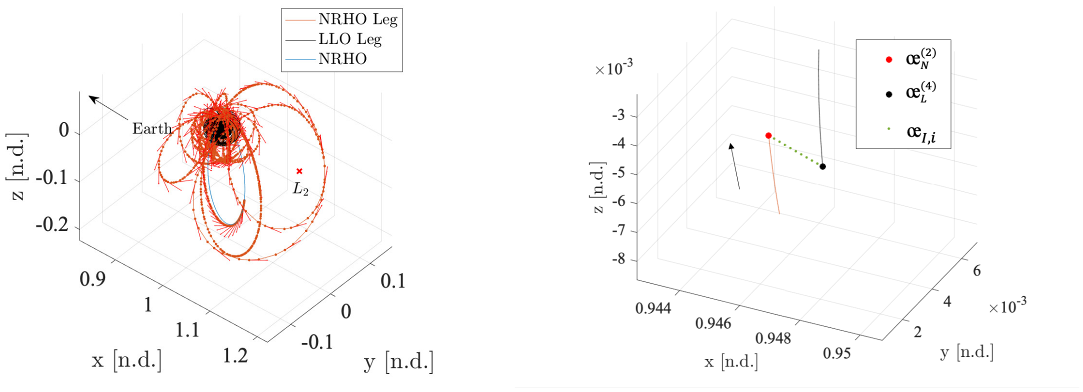

(a) Discretization [C1]

(b) Continuation scheme [C2]

Figure 9: Illustration of steps [C1] and [C2]

"optimal" trajectory depends on the set tolerance, where optimizing with a tight tolerance often requires longer computation time. Also, the optimization takes place only within the assumed dynamical model, CR3BP. For an actual flight, optimization within a higher-fidelity model with realistic constraints is required. For these reasons, in the current investigation, the optimization is remains an optional step.

RESULTS

The results from the algorithm are first demonstrated with two sample LLOs. Two sets of LLOs in Table 4 represent previously considered science orbits for the LIC mission for the surface exploration of the Moon. Note that the orbital elements are originally defined within the J2000 frame but are first transitioned into the CR3BP inertial frame for the current analysis. The main source of the discrepancy for a, e is the varying distance between the primaries,[18] and the deviation for Ω, i is associated with the fact that the fundamental plane of J2000 frame is defined with respect to the Earth mean equatorial (EME) plane while the that of the Earth-Moon CR3BP inertial frame is tilted with respect to the EME plane.

Figure 10 illustrates the feasible solutions corresponding to these two exemplary LLOs. The plots in the first row demonstrate the end-to-end transfer trajectory within the Earth-Moon CR3BP rotating frame. The plots in the second row illustrate the same transfers in the Moon-centered inertial frame, where the inertial states are obtained by the transformation process with $\tau = \tau_F$ as the reference epoch. In the third row, zoomed-in views in the inertial frame are depicted near the Moon to denote the location of the interface between the NRHO and LLO legs. Consistent with the previous investigations,[6,8] the orbital plane of the transfer arc within the inertial frame appears to be "inertially locked", or nearly constant after a captured motion starts to occur, as the thrust direction employed by the anti-velocity law mainly changes the energy but not the orbital plane. The thrust histories for the NRHO legs are illustrated in Figures 10(g)-10(h), where the dotted lines denote the maximum level of thrust, 1.1mN. Recall that the initial guess for the NRHO leg assumes the thrust at 90% of the maximum thrust level. The deviation corresponds to the result from the corrections process; the thrust history is adjusted to meet the continuity constraint at the interface. Also note that the initial guess is generated with a control law tuple, **S**, that utilizes either anti-velocity or pro-velocity laws. The converged thrust history still demonstrates this tendency, where significant portions of the thrust are exerted in the direction aligned with or opposite to $\hat{v}$, colored in red. The optimal solution nearly exhibits the similar geometry as the feasible solution and is not included, although the thrust history demonstrates a bang-bang behavior that results from the optimization process (Figure 11). A tolerance of 1×10^{-7} is utilized for the optimality tolerance within the optimizer. The costs for the feasible as well as optimal trajectories for these sample LLOs are included in Table 5. The costs include the consumed propellant, $\Delta\tilde{m} = \tilde{m}_0 - \tilde{m}_F$, the equivalent ΔV, computed as $\tilde{I}_{sp}\tilde{g}_0 \log(\tilde{m}_0/\tilde{m}_F)$, and the total time of flight, $TOF = t_2 + t_3 + t_{D,N} + t_B + t_{D,L}$, in days. Note that although the low-thrust engine does not provide an impulsive burn, i.e., instantaneous change in the velocity, the equivalent ΔV is computed for reference. The costs for each leg, and the total costs are provided. Note that the optimized trajectories are associated with the same time of flight compared to the feasible trajectories, as the optimization process only optimizes the propellant consumption.

Table 4: Sample LLOs

	LLO 1[4]		LLO 2	
Frame	J2000	CR3BP	J2000	CR3BP
a_F [km]	4287.4	4073.3	3502.7	3378.8
e_F [n.d.]	0.5714	0.5716	0.3883	0.3883
i_F [deg]	56	45	84	84
Ω_F [deg]	65	85	280	276
ω_F [deg]	355	323	170	197.5
Epoch	06-May-2022	$\tau_F = 103°$	26-Aug-2022	$\tau_F = 148°$

Table 5: Costs comparison

Legs	Costs	LLO 1		LLO2	
		Feasible	Optimized	Feasible	Optimized
NRHO Leg	m [kg]	0.315	0.299	0.262	0.252
	ΔV [m/s]	0.496	0.470	0.411	0.395
	TOF [days]	78		75	
LLO Leg	m [kg]	0.346		0.383	
	ΔV [km/s]	0.558	0.557	0.616	0.616
	TOF [days]	77		85	
Total	m [kg]	0.661	0.645	0.645	0.635
	ΔV [km/s]	1.054	1.027	1.027	1.011
	TOF [days]	155		160	

Range of the Targetable LLOs

Besides two sample LLOs, the proposed framework is tested over multiple LLOs and arrival epochs to analyze the range of the LLOs that are targetable by the algorithm. To systematically define different LLOs, a grid is constructed over e_F, i_F, ω_F values, where four values of e_F are equally placed between 0.1 and 0.55, i between $0.01°$ and $90°$ with 5 equally divided points, and ω between $0°$ and $288°$ with 5 equally divided points. Recall that the step [B3] locates a candidate NRHO leg from the the data set generated with different **S** that results in minimum distance for e, i, ω. Some combinations of these orbital elements are only scarcely covered by the data set, and the formulated grid serves to locate the regions where the data set fails to provide NRHO legs that are sufficiently close to LLO legs. The rest of the values for the inputs assumes $a_F = 5000$km, $\Omega_F = \tau_F = 0°$. Then, nine different cases, each corresponding to $4 \cdot 5 \cdot 5 = 100$ points within the grid, are formulated by changing one of a_F, Ω_F, and τ_F while fixing the rest of the variables; 3000km and 5000km are utilized for a_F, and $90°, 180°, 270°$ are utilized for Ω_F and τ_F values, amounting to $9 \cdot 100 = 900$ trial runs in total.

Overall, out of 900 test runs, 694 runs converged, resulting in 77% of success ratio. The results are summarized with the scatter plot, depicted in Figure 12. Each dot in the plot corresponds to 9 total cases for each grid point constructed with different a_F, Ω_F and τ_F values. The numbers of successful runs, out of 9, are recorded where the yellow dots denote the maximum possible successful runs and the red dots indicate the opposite. The only step within the algorithm where it fails is step [C2] in Figure 8, solving for the trajectory that satisfies $\text{œ}_N = \text{œ}_L$. The steps leading to [C2] consists of generating an initial guess and discretizing the NRHO leg, where no particular challenge is noted. Recall that within step [C2], the error vector $\Delta\text{œ}$ is gradually decreased to zero by solving for intermediate terminal states, shown as $\text{œ}_{I,i}$ in Figure 9(b). When the error provided by the initial guess is too large, the thrust history easily saturates, i.e., the thrust magnitude is at its maximum value for most portions of the NRHO leg and further corrections cannot take place. One such example is illustrated in Figure 13, where the thrust history of a failing case is plotted. Here, the gradient-based method fails to further correct to œ_L, and stops where $\text{œ}_{I,i} = 0.85\Delta\text{œ} + \text{œ}_N^{(4)}$, i.e., it only overcomes the error at the interface by 85% of the required amount. Other failing runs report similar behavior in the thrust history, where the saturation occurs. While overall convergence behavior depends on the low-

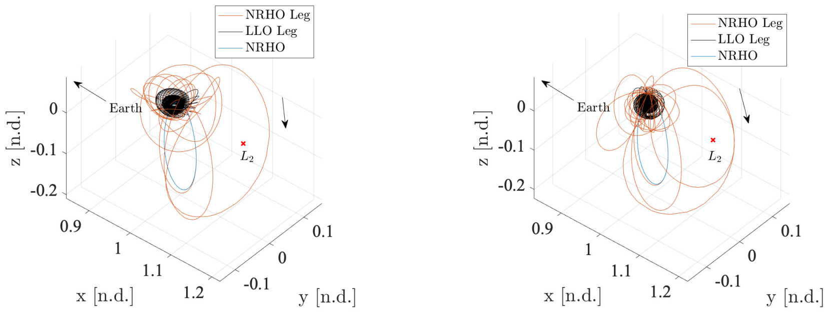

(a) Rotating frame view (to LLO 1) (b) Rotating frame view (to LLO 2)

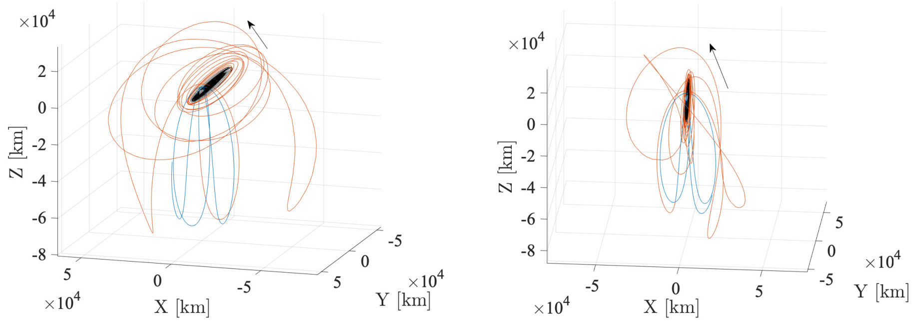

(c) Inertial frame view (to LLO 1) (d) Inertial frame view (to LLO 2)

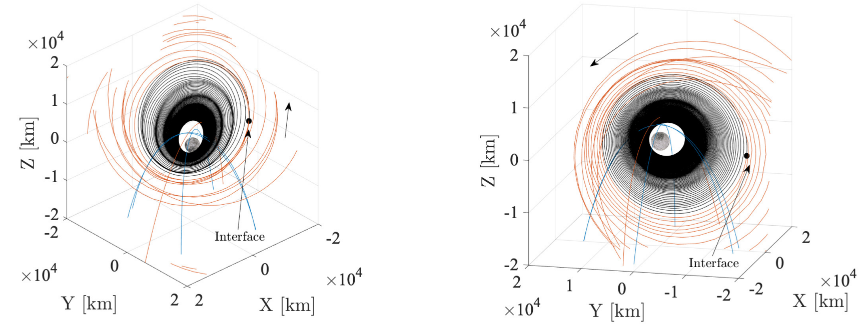

(e) Ineritial frame view (to LLO 1, zoomed) (f) Inertial frame view (to LLO 2, zoomed)

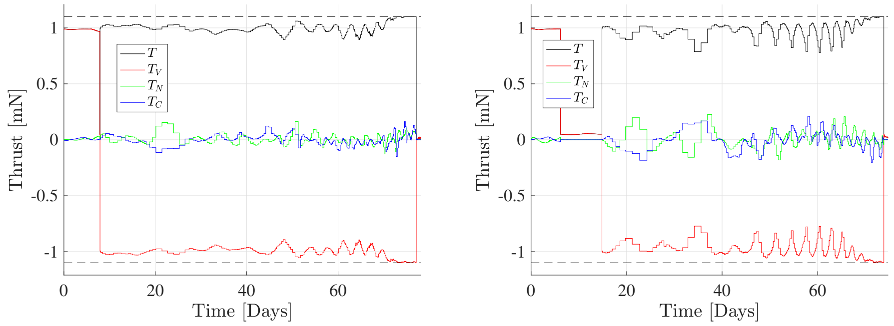

(g) Thrust history (to LLO 1) (h) Thrust history (to LLO 2)

Figure 10: Feasible trajectories from the algorithm for the sample LLOs

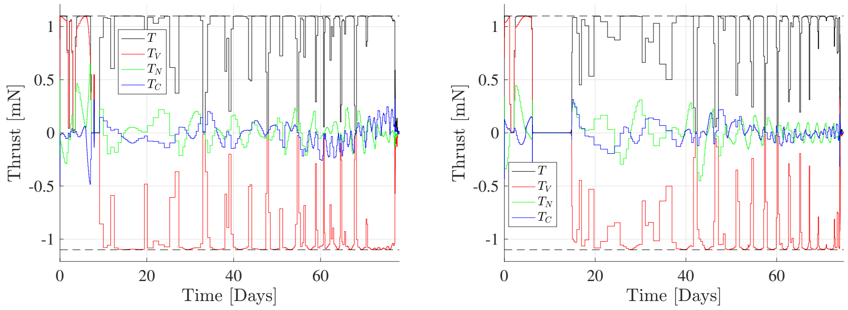

(a) Thrust history (to LLO 1)

(b) Thrust history (to LLO 2)

Figure 11: Thrust histories of optimized trajectories for the sample LLOs

thrust related parameters (Table 3), the maximum acceleration level provided by the engine ($\tilde{T}_{max}/\tilde{m}_0$) is directly related to the control authority and has a great influence on the performance; for a bigger maximum acceleration level, the framework is likely to demonstrate better convergence behavior.

Figure 12 exhibits two broad regions where the framework fails to provide feasible solutions. The LLOs with large e_F and high i_F, as well as LLOs with small e_F and low i_F are two challenging regions. This deficiency is not addressed in the current, preliminary analysis. On the contrary, LLOs with intermediate i, between 20° and 60°, are far more reliably targeted by the framework, succeeding in most runs for the test cases. As the error vector is six dimensional, where each component of œ influences the behavior of the framework in a coupled way, it is challenging to represent the error with single scalar metric. It is further compounded by the fact that matrix algebra with large dimensions within the gradient-based methods is not directly controllable by the user from outside. As a result, somewhat random behavior is observed, where an obvious distinction of the regions of LLOs is not readily available.

However, partial insight is available by analyzing the error vector components from the test runs. Figure 14 includes six box plots, one for each orbital element, where the x-axes of the plots indicate different steps within the algorithm, and the y-axes correspond to the magnitudes of the error for each orbital element. Black and red indicate the success (S) and failure (F) runs, respectively. The first kind of error is defined as $\Delta \text{œ}_1 = \text{œ}_L^{(2)} - \text{œ}_N^{(1)}$ from [B3]. This error is related to the inability of the data set to cover certain combinations of e, i, ω values at the interface. The second kind of error is defined as $\Delta \text{œ}_2 = \text{œ}_L^{(3)} - \text{œ}_N^{(2)}$ from steps [B4-B5], where the main source of error originates from the ballistic propagation in the Earth-Moon CR3BP for t_B that perturbs the orbital elements of the NRHO leg at the interface. The final kind of error is defined as $\Delta \text{œ}_3 = \text{œ}_L^{(4)} - \text{œ}_N^{(2)}$ from step [B6] that occurs by updating the arrival location along the LLO, ν_F. Then, the total error provided by the initial guess generation phase ([B1-B6]) amounts to $\Delta \text{œ} = \Delta \text{œ}_4 = \Delta \text{œ}_1 + \Delta \text{œ}_2 + \Delta \text{œ}_3$, where $1 - 4$ are marked at the x-axes in Figure 14. Note that the errors in Ω and ν are first introduced in $\Delta \text{œ}_2$ and $\Delta \text{œ}_3$, respectively.

The box plots offer insight regarding which steps each component of the error is accumulated in. Also, by looking at the difference of overall tendency of the errors for the success and fail runs, measured by the vertical location of the black and red boxes, respectively, the level of the error that results in fail runs is estimated. The central mark indicates the median, and the bottom and top edges of the box indicate the 25th and 75th percentiles. Note, however, that many outliers exist for the successful cases that are associated with large errors, implying that the magnitude of each component of the $\Delta \text{œ}$ is only an indirect indicator of the success of the algorithm.

Costs Estimation

The estimation on the costs for the transfers, measured by the propellant consumption and the time of flight, is provided to illustrate the performance of the proposed framework. The costs are separately computed for the NRHO and LLO legs. For the NRHO leg, the costs are mostly indicated by the values from the data

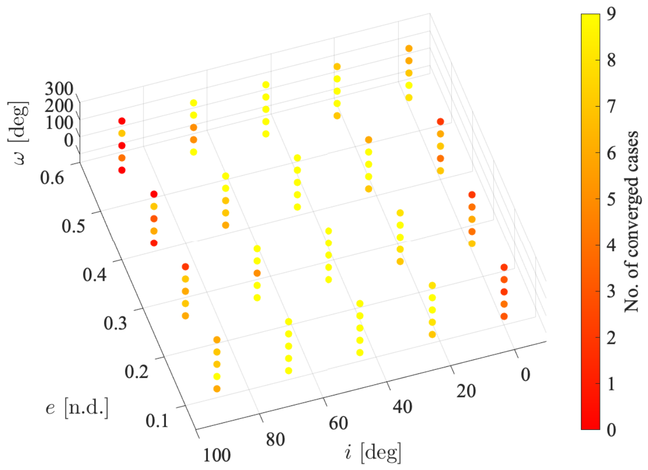

Figure 12: Range of the LLOs

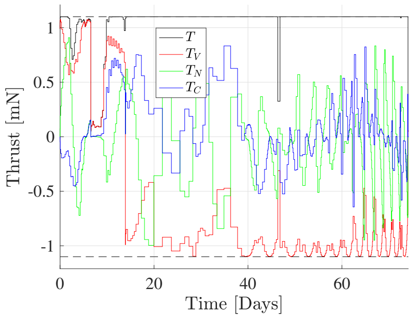

Figure 13: Thrust saturation

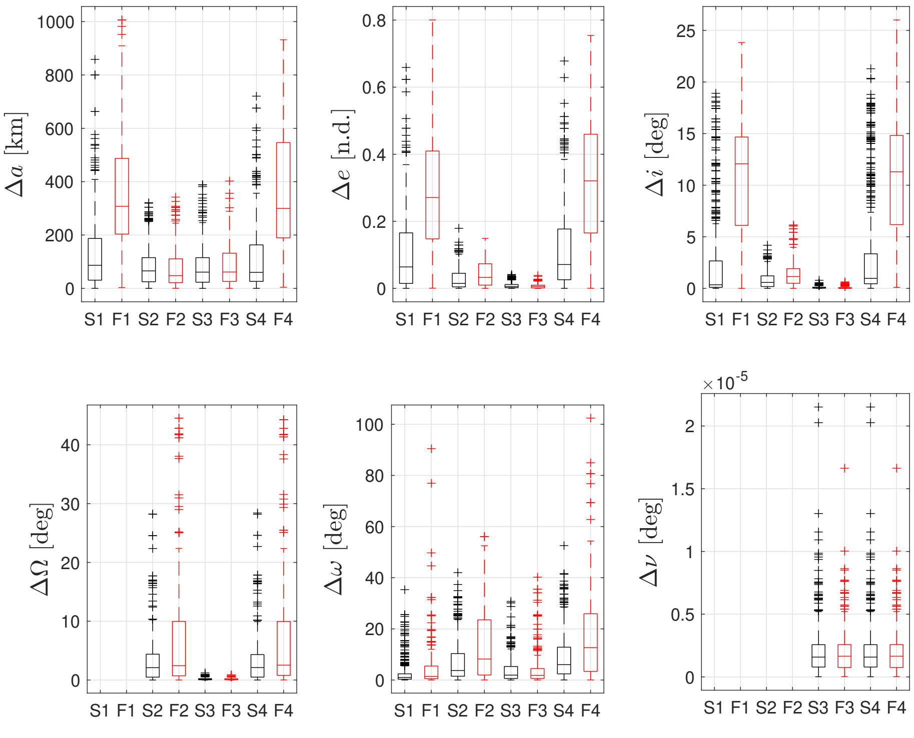

Figure 14: Errors $(\Delta œ_1, \Delta œ_2, \Delta œ_3, \Delta œ_4)$ accumulated within the initial guess generation phase of the framework

set generated with $\mathbf{S}$, as the subsequent process within the framework depends heavily on the initial guess from the data set and only marginally changes the costs. Figures 15(a) and 15(b) describe the cost maps of the data set generated with $\mathbf{S}$. For the propellant consumption, the maximum and minimum values of the consumed propellant are approximately 0.23kg and 0.39kg, respectively. This value is slightly modified within the framework after the initial guess for the NRHO leg is converged for feasibility, i.e., continuity at the interface. For the cases that converge successfully to the target LLO, the propellant consumption varies from the initial guess value from the data set by minimum of -2% to maximum of $+14\%$, where the average variation is $+2\%$. Note that solving for a feasible trajectory often results in consuming more propellant as the corrector tends to utilize the gap between the 90% thrust and the maximum level of thrust. For the time of flight defined as $TOF = t_2 + t_3 + t_{D,N}$, the minimum and maximum time of flight retrieved from the data set are 80 days and 160 days, respectively. A subset of the data set may be utilized to locate only the candidate NRHO legs that satisfy certian costs constraints. For instance, NRHO legs with $\Delta\tilde{m} < 0.3$kg may be selected to serve as the subset to represent cost-efficient transfer options.

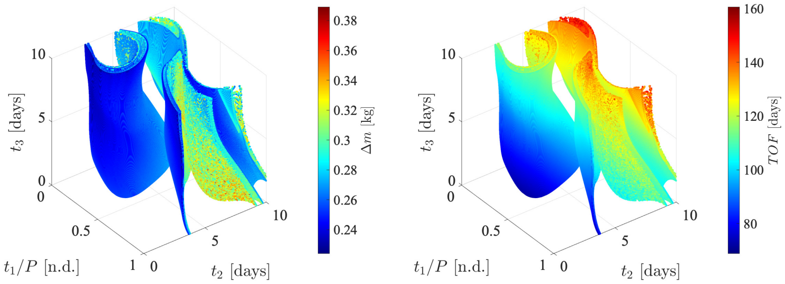

(a) Mass contour plot

(b) TOF contour plot

Figure 15: Contour plots for NRHO leg data set

The costs for the LLO leg depend on its orbital elements but also on τ_F and m_F values. The most decisive element, however, is a_F, as a significant amount of thrust is required to correct for the energy gap that exists between the LLO and the interface at $JC = 3.3$. The reference values are computed as the average costs computed from the test runs for $a = 4000\text{km}, 5000\text{km}$, and 6000km that converge. The corresponding reference values are listed in table 6.

Table 6: LLO leg reference costs

	$a = 4000$ [kg]	$a = 5000$ [kg]	$a = 5000$ [kg]
$\Delta\tilde{m}$ [kg]	0.33	0.26	0.21
TOF [days]	75	60	50

CONCLUDING REMARKS

A low-thrust trajectory design framework is proposed within the Earth-Moon CR3BP for the transfers between the 9:2 NRHO to multilple LLOs that serve as potential science orbits for the Moon. A targeting problem that involves a forward propagation from the NRHO and a backward propagation from an LLO is constructed. Then, a series of steps are devised to generate initial guesses with minimal discontinuity at the interface, later to be converged to feasible as well as optimal trajectories. The framework is tested over various LLOs, where the range of the targetable LLOs as well as the costs of the transfer arcs are provided.

ACKNOWLEDGEMENTS

This investigation has been accomplished in collaboration with NARA Goddard Space Flight Center under Grant Number 80NSSC20K1117. The authors also thank the Purdue University College of Engineering as well as the School of Aeronautics and Astronautics, for support and access to the Rune and Barbara Eliasen Visualization Laboratory. Additionally, many thanks to the members of the Purdue Multi-Body Dynamics Research Group for interesting discussions and ideas. Special thank you to Nicholas Lafarge and Rolfe Power for sharing the C++ codes.

REFERENCES

[1] J. C. Crusan, R. M. Smith, D. A. Craig, J. M. Caram, J. Guidi, M. Gates, J. M. Krezel, and N. B. Herrmann, "Deep Space Gateway Concept: Extending Human Presence into Cislunar Space," *2018 IEEE Aerospace Conference*, IEEE, 2018, pp. 1–10.

[2] P. Clark, B. Malphrus, K. Brown, D. Reuter, R. MacDowall, D. Folta, A. Mandell, T. Hurford, C. Brambora, D. Patel, *et al.*, "Lunar Ice Cube Mission: Determining Lunar Water Dynamics with a First Generation Deep Space CubeSat," *47th Lunar and Planetary Science Conference*, Vol. 330, 2016, pp. 463–468.

[3] "Advanced Space, LLC, Webpage," `https://advancedspace.com/`. Accessed: 2021-04-29.

[4] B. P. Pino, R. Pritchett, K. C. Howell, and D. C. Folta, "Extended Mission Options for the Lunar IceCube Low-Thrust Spacecraft by Leveraging the Dynamical Environment," *Proceedings of the International Astronautical Congress, IAC*, Vol. 2020-Octob, No. October, 2020, pp. 12–14.

[5] M. Rozek, H. Ogawa, S. Ueda, T. Ikenaga, *et al.*, "Multi-Objective Optimisation of NRHO-LLO Orbit Transfer Via Surrogate-Assisted Evolutionary Algorithms," *AIAC18: 18th Australian International Aerospace Congress (2019)*, Engineers Australia, Royal Aeronautical Society., 2019, p. 1001.

[6] R. J. Whitley, D. C. Davis, L. M. Burke, B. P. McCarthy, R. J. Power, M. L. McGuire, and K. C. Howell, "Earth-Moon Near Rectilinear Halo and Butterfly Orbits for Lunar Surface Exploration," *AAS/AIAA Astrodynamics Specialists Conference, Snowbird, Utah*, 2018.

[7] L. Lu, H. Li, W. Zhou, and J. Liu, "Design and Analysis of a Direct Transfer Trajectory from a Near Rectilinear Halo Orbit to a Low Lunar Orbit," *Advances in Space Research*, Vol. 67, No. 3, 2021, pp. 1143–1154.

[8] J. F. Horton, T. Kokan, C. R. Joyner, D. Morris, and R. Noble, "Lunar Landing and Sample Return from Near Rectilinear Halo Orbit Using High-Powered Solar Electric Propulsion," *Advances in the Astronautical Sciences*, Vol. 169, No. February, 2019, pp. 487–497.

[9] R. E. Pritchett, *Strategies for Low-Thrust Transfer Design Based on Direct Collocation Techniques*. Ph.D. Dissertation, Purdue University, West Lafayette, Indiana, 2020.

[10] E. M. Zimovan-Spreen, *Trajectory Design and Targeting for Applications to the Exploration Program in Cislunar Space*. Ph.D. Dissertation, Purdue University, West Lafayette, Indiana, 2021.

[11] A. D. Cox, K. C. Howell, and D. C. Folta, "Dynamical structures in a low-thrust, multi-body model with applications to trajectory design," *Celestial Mechanics and Dynamical Astronomy*, Vol. 131, No. 3, 2019, pp. 1–34.

[12] A. D. Cox, *A Dynamical Systems Perspective For Preliminary Low-Thrust Trajectory Design In Multi-Body Regimes*. Ph.D. Dissertation, Purdue University, West Lafayette, Indiana, 2020.

[13] A. Petropoulos, "Low-Thrust Orbit Transfers Using Candidate Lyapunov Functions with a Mechanism for Coasting," *AIAA/AAS Astrodynamics Specialist Conference and Exhibit*, 2004, p. 5089.

[14] D. Canales, M. Gupta, B. Park, and K. Howell, "Exploration of Deimos and Phobos Leveraging Resonant Orbits," *31st AAS/AIAA Space Flight Mechanics Meeting*, Charlotte, North Carolina (Virtual), 2021.

[15] J. Shannon, M. Ozimek, J. Atchison, and C. Hartzell, "Rapid Design and Exploration of High-Fidelity Low-Thrust Transfers to the Moon," *2020 IEEE Aerospace Conference*, IEEE, 2020, pp. 1–12.

[16] D. C. Davis, R. J. Power, K. C. Howell, and J. P. Gutkowski, "Lunar Impact Probability for Spacecraft in Near Retilinear Halo Orbits," *31st AAS/AIAA Spaceflight Mechanics Meeting*, Charlotte, North Carolina (Virtual), 2021.

[17] V. Muralidharan, *Stretching Directions in Cislunar Space: Stationkeeping and an Application to Transfer Trajectory Design,*. Ph.D. Dissertation, Purdue University, West Lafayette, Indiana, 2021.

[18] B. Park, "Low-Thrust Trajectory Design for Tours of the Martian Moons," M.S. Thesis, Purdue University, West Lafayette, Indiana, 2021.

[19] A. Wächter and L. T. Biegler, "On the Implementation of an Interior-Point Filter Line-Search Algorithm for Large-Scale Nonlinear Programming," *Mathematical programming*, Vol. 106, No. 1, 2006, pp. 25–57.